Planetary and Space Science 115 (2015) 57–63

Contents lists available at ScienceDirect

Planetary and Space Science

journal homepage: www.elsevier.com/locate/pss

Imaging the South Pole–Aitken basin in backscattered neutral hydrogen atoms

A. Vorburger [a,*], P. Wurz [b], S. Barabash [c], M. Wieser [c], Y. Futaana [c], A. Bhardwaj [d], K. Asamura [e]

[a] Division of Physical Sciences, American Museum of Natural History, New York, USA
[b] Physikalisches Institut, Universität Bern, Sidlerstrasse 5, CH-3012 Bern, Switzerland
[c] Swedish Institute of Space Physics, Box 812, SE-98128 Kiruna, Sweden
[d] Space Physics Laboratory, Vikram Sarabhai Space Center, Trivandrum 695 022, India
[e] Institute of Space and Astronautical Science, 3-1-1 Yoshinodai, Sagamihara, Japan

ARTICLE INFO

Article history:
Received 29 August 2014
Received in revised form
4 January 2015
Accepted 11 February 2015
Available online 21 February 2015

Keywords:
Moon
South Pole–Aitken basin
Energetic neutral atoms
Backscattering

ABSTRACT

The lunar surface is very efficient in reflecting impinging solar wind ions as energetic neutral atoms (ENAs). A global analysis of lunar hydrogen ENAs showed that on average 16% of the solar wind protons are reflected, and that the reflected fraction can range from less than 8% to more than 24%, depending on location. It is established that magnetic anomalies reduce the flux of backscattered hydrogen ENAs by screening-off a fraction of the impinging solar wind. The effects of the surface properties, such as porosity, roughness, chemical composition, and extent of weathering, were not known.

In this paper, we conduct an in-depth analysis of ENA observations of the South Pole–Aitken basin to determine which of the surface properties might be responsible for the observed variation in the integral ENA flux. The South Pole–Aitken basin with its highly variable surface properties is an ideal object for such studies. It is very deep, possesses strikingly elevated concentrations in iron and thorium, has a low albedo and coincides with a cluster of strong magnetic anomalies located on the northern rim of the basin. Our analysis shows that whereas, as expected, the magnetic anomalies can account well for the observed ENA depletion at the South Pole–Aitken basin, none of the other surface properties seem to influence the ENA reflection efficiency. Therefore, the integral flux of backscattered hydrogen ENAs is mainly determined by the impinging plasma flux and ENA imaging of backscattered hydrogen captures the electrodynamics of the plasma at the surface. We cannot exclude minor effects by surface features.

1. Introduction

The Moon, not being protected by a global magnetic field nor by an atmosphere, is constantly bombarded by solar wind ions. Until a few years ago, it was commonly assumed that the impinging solar wind ions are almost completely absorbed by the lunar surface (e.g. Crider and Vondrak, 2002; Feldman et al., 2000). This assumption has been invalidated by several recent observations conducted by Nozomi (Futaana et al., 2003), Kaguya (Saito et al., 2008), Chandrayaan-1 (Wieser et al., 2009; Lue et al., 2011), the Interstellar Boundary Explorer (IBEX) (McComas et al., 2009), Chang'E-1 (Wang et al., 2010) and Artemis (Halekas et al., 2013).

In particular, observations by Kaguya and Chandrayaan-1 showed that in fact on average between 0.1% and 1% of the impinging solar wind ions are reflected back from the lunar surface as ions, with local values ranging from 0% to more than 50% (Saito et al., 2008; Lue et al., 2011). Moreover, IBEX and Chandrayaan-1 observations showed that on average 16% of the impinging solar wind protons are backscattered as neutral hydrogen atoms from the lunar surface (McComas et al., 2009; Wieser et al., 2009; Vorburger et al., 2013). Mapping of the complete Chandrayaan-1 dataset showed that this backscatter percentage can range from less than 8% to more than 24% (Vorburger et al., 2013).

While an in-depth analysis of several observations of local magnetic anomalies showed that these influence the amount of solar wind flux reaching the lunar surface (e.g. Lin et al., 1998; Wieser et al., 2010; Saito et al., 2010; Lue et al., 2011; Vorburger et al., 2012), influences of other surface properties on the ion–surface interaction have not been investigated. We thus chose to analyze the ENA measurements in a region that exhibits very distinct features in as many surface properties as possible.

* Corresponding author. Tel.: +1 212 796 5082.
E-mail address: avorburger@amnh.org (A. Vorburger).

http://dx.doi.org/10.1016/j.pss.2015.02.007
0032-0633/

With the South Pole–Aitken basin exhibiting distinct variability of several properties potentially affecting the ion–surface interaction (visible albedo, topography, chemistry, mineralogy, magnetism), it poses a choice location for analyzing the interaction between the solar wind and the lunar surface. By comparing an ENA integral flux map to variations in the different maps, we can determine what surface properties ENAs are sensitive to. This helps us to shed more light onto the still poorly understood backscattering process of plasma ions from regolith covered planetary surfaces.

The role of crustal magnetic fields on the lunar surface for the observation of these ENAs is that the plasma physical interaction of the solar wind plasma with the surface magnetic fields governs actual access of ions to the surface, as has been demonstrated in several papers before (Vorburger et al., 2012, 2013). Scattering of atoms and ions at solid surfaces is a complex process where the interaction of the impinging particles with the surface atoms is determined by the topmost surface of the solid, its chemical composition, and its roughness (Niehus et al., 1993). Variations in visible albedo of the Moon can have several causes, for example an increased roughness of the surface at scales commensurate with optical wavelengths can cause a lower visible albedo or a different chemical (or mineralogical) composition. Both of these effects will cause differences in the particle scattering from the surfaces: increased roughness will reduce the efficiency of particle reflection to space because of multiple scattering at the fractal surfaces and higher probability of absorption of a particle, and a different chemical composition changes the scattering partners for the reflection since this interaction is to first order a single or a few binary collisions. The South-pole Aitken basin is the oldest recognized topographical feature on the lunar surface. With its size of about 2500 km and a depth of about 12 km it indicates that a substantial amount of material has been removed from the surface during the impact forming this basin. Thus, the material on the floor of this basin might be different from the material outside this basin. The chemical and mineralogical composition of the South-pole Aitken basin is different from typical highland regions, as recorded in data from the Galileo, Clementine and Lunar Prospector missions (e.g. Lawrence et al., 1998, 2002), thus possibly affecting the ENA albedo. In terms of mineralogy, the basin floor is much richer in clinopyroxene (monoclinic crystal) and orthopyroxene (orthorhombic crystals) minerals than the surrounding highlands that are largely anorthositic (mostly plagioclase feldspar with minor mafic contributions). Pyroxenes are Si- or Al-oxide based minerals with ions of Ca, Na, Mg, Fe and other elements, many of heavier mass than in the anorthositic highlands, again, which might affect the ENA albedo. The remote sensing observations indicate that the floor of this basin has slightly elevated abundances of iron, titanium, and thorium. The enrichment in several heavier elements, which may represent lower crust material, will affect the particle scattering properties.

In Section 2 we briefly describe the instrument and the observations that were used for this analysis. In Section 3 we discuss the different surface features in which the South Pole–Aitken basin is distinguished from the surrounding terrain, and present two maps showing the ENA observations of that region. In Section 4 we thoroughly discuss the correlation between the ENA map and local surface features and thus deduced implications as to what mechanisms can cause the observed ENA depletions. Section 5 presents our conclusions and discusses where else our results might be applicable.

2. Observations and instrumentation

For this study we analyzed measurements conducted by the Chandrayaan-1 Energetic Neutrals Analyzer (CENA) (Kazama et al., 2007), which is a part of the Sub-keV Atom Reflecting Analyzer (SARA) instrument (Bhardwaj et al., 2005; Barabash et al., 2009) on board Chandrayaan-1 (Goswami and Annadurai, 2009). CENA measured ENAs originating from the lunar surface within the energy range 10 eV to 3.3 keV and with an energy resolution of $\Delta E/E \approx 50\%$. Even though CENA allows crude mass analysis to identify H, He, and O (Vorburger et al., 2014), we only analyzed hydrogen measurements in this study because the hydrogen counts by far exceed the counts in all other mass bins combined, thus they offer the statistically most robust measurement by far. CENA's field-of-view is spanned by seven angular sectors, which provide information about the arrival direction of the measured ENAs. The central sector is nadir pointing, i.e., its bore-sight crosses the lunar surface at the sub-spacecraft point. The other six sectors are symmetrically arranged around the central sector in the azimuth direction covering a swath of the full size of the Moon perpendicular to the orbit motion (see Fig. 1 in Wieser et al., 2010 for an illustration). Measurements by the outermost two sectors were disregarded in this study because they not only record measurements from the lunar surface but also from the lunar limb. The surface projections of the remaining five sectors are given in Table 1.

The Chandrayaan-1 mission operated from October 2008 until the end of August 2009. The spacecraft's circular polar orbit was initially set at an altitude of 100 km and was raised to 200 km at the end of May 2009. Discarding the period when the Moon was inside Earth's magnetosphere, we were left with 163 orbits, 64 of which passed directly over the South Pole–Aitken basin (i.e. the instrument's boresight crossed the South Pole–Aitken basin). Since each orbit gives us 5 datasets (one for each angular sector), we had in total 815 datasets to analyze, about 250 of which contained measurements from the South Pole–Aitken basin.

3. The South Pole–Aitken basin

3.1. The South Pole–Aitken basin in ENAs

Fig. 1 shows two different ENA reflection ratio maps centered on the South Pole–Aitken basin. The reflection ratio is defined as the ratio of ENA flux backscattered from the lunar surface for CENA's complete energy range and all exit angles (hemisphere) to the impinging solar wind ions:

$$R = \frac{J_{ENA}}{J_{SW}}, \tag{1}$$

where J_{ENA} is the reflected ENA flux over the zenith hemisphere (the 2π sphere) and J_{SW} is the impinging solar wind flux observed at the Moon. The solar wind values were taken from the WIND spacecraft time-shifted according to the distance between WIND and Chandrayaan-1 as well as the plasma's velocity.

Since a single ENA observation is only able to measure the flux backscattered in a certain direction (i.e., towards the instrument's field of view), we first had to deduce the total ENA flux released over the complete zenith hemisphere (J_{ENA}) from the directional measurement ($j_{ENA}(SZA, \phi, \theta)$). This was accomplished by fitting the measurements with the scattering function presented in

Table 1
Surface projections of the central five sectors given in lunar longitude/latitude as well as kilometers for two nominal spacecraft altitudes (100 km and 200 km).

Sector	lon × lat @ 100 km	lon × lat @ 200 km	km × km @ 100 km	km × km @ 200 km
1	5.57° × 0.36°	13.72° × 0.76°	169 × 11 km^2	416 × 23 km^2
2	3.20° × 0.36°	6.53° × 0.76°	97 × 11 km^2	198 × 23 km^2
3	2.74° × 0.36°	5.54° × 0.76°	83 × 11 km^2	168 × 23 km^2
4	3.20° × 0.36°	6.53° × 0.76°	97 × 11 km^2	198 × 23 km^2
5	5.57° × 0.36°	13.72° × 0.76°	169 × 11 km^2	416 × 23 km^2

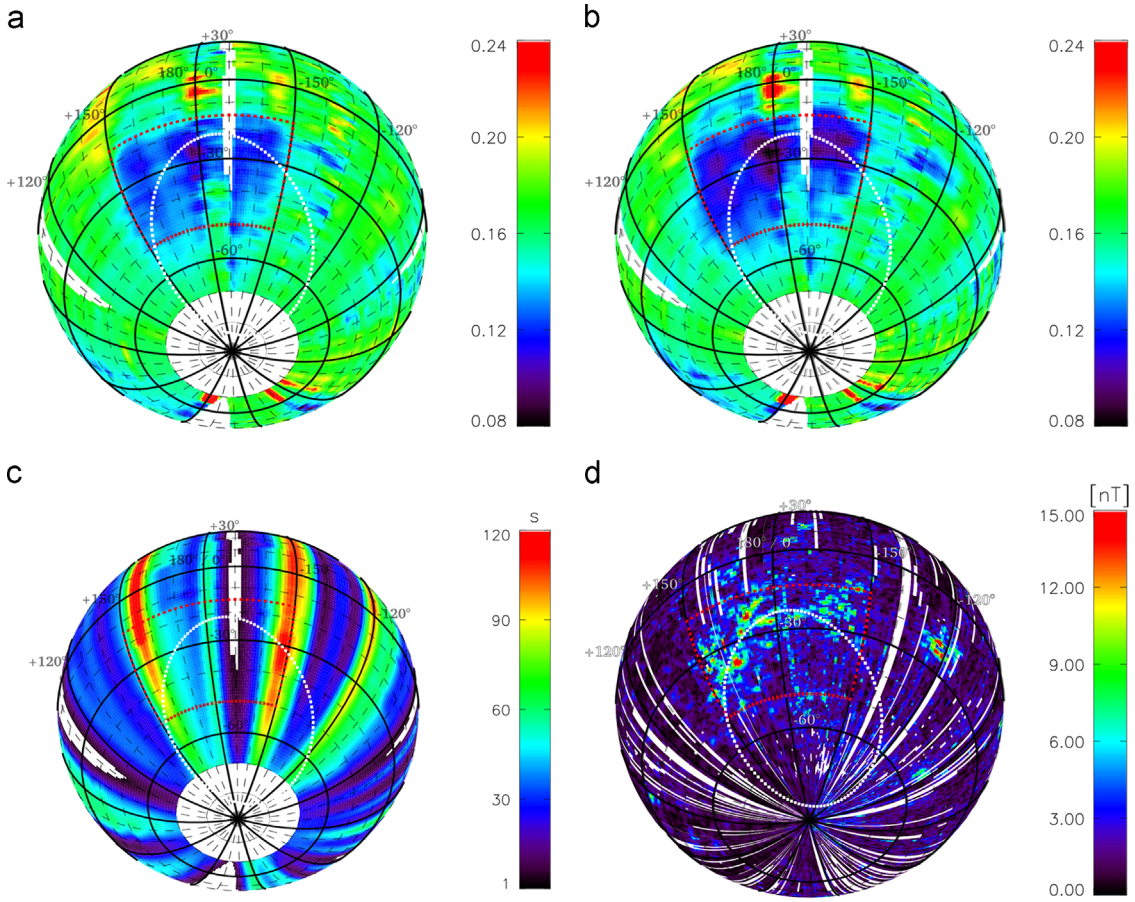

Fig. 1. ENA maps with focus on the South Pole–Aitken basin. The two different ENA reflection ratio maps depict the reflection ratios in the low energy range (panel a) and in the high energy range (panel b) separately. Also shown is the effective exposure time (see text for details; panel c) and the map showing the magnetic field at 30 km altitude as measured by Lunar Prospector (panel d). The approximate extension of the ENA feature is described by the red polygon, whereas the ellipse fitting the topography data best is over-plotted in white.

Appendix A in Vorburger et al. (2013), which gives for every angle of incidence of the solar wind ions the angular distribution of the backscattered ENA flux. Eq. (1) thus becomes

$$R = \frac{j_{\mathrm{ENA}}(\mathrm{SZA}, \phi, \theta)}{J_{\mathrm{SW}} \cdot f_S(\mathrm{SZA}, \phi, \theta)}, \tag{2}$$

where $j_{\mathrm{ENA}}(\mathrm{SZA}, \phi, \theta)$ is the directional ENA flux, and where $f_S(\mathrm{SZA}, \phi, \theta)$ is the directional scattering function. To compensate for the intrinsically low number of counts towards the poles, we applied the same flat-field correction as described in Vorburger et al. (2012). Once we computed the reflection ratio for each individual measurement, we combined all measurements into a single map. We decided to divide the map into two energy ranges to see if variations present in the ENA maps depend on the energy of the reflected atoms with respect to the impacting protons. Fig. 1 panel a shows the lower half of the energy range (ENAs with energies $< 30\%$ of the energy of the currently impinging solar wind plasma) and panel b shows the upper half of the energy range (ENAs with energies $> 30\%$ of the energy of the currently impinging solar wind plasma). The red polygons in both panels denote the approximate extension of the ENA feature. In addition, we over-plotted the topographic structure of the South Pole–Aitken basin in white (see text below). Fig. 1 panel c shows the effective exposure time for each point on the surface. To correct for the non-uniform angular response of each sector, the total exposure time of 4 s of each measurement was multiplied with a two-dimensional Gaussian distribution covering the given sector's surface projected field of view. The effective exposure time in Fig. 1 panel c is the sum of all of these fractions. When plotting the data we required a minimal exposure time of 1 s, to ensure that the statistics are sufficient. In addition, due to the steep decrease in counting statistics towards the polar regions, we cut off data below -70° and above 70° latitude. Fig. 1 panel d shows for comparison the magnetic field magnitude at 30 km altitude as measured by Lunar Prospector.

3.2. The South Pole–Aitken basin in other features

The South Pole–Aitken basin is the most pronounced topographic structure on the Moon. The highly degraded appearance and a large number of superimposed craters suggest that it may be the oldest basin on the Moon. It is located at (180°E, 56°S), has a diameter of about 2500 km, and is approximately 12 km deep (McFadden et al., 2007). Topography and gravity measurements imply that whereas the lunar crust has an average thickness of about 50 km, the crust is reduced to a thickness of about 15 km within the basin (Wieczorek et al., 2012). A global albedo map from the 750-nanometer filter of the Clementine UV-VIS camera shows that the South Pole–Aitken basin is also distinguishable by eye as a dark mafic anomaly (Lee et al., 2009). In addition, the South Pole–Aitken basin differs compositionally from the surrounding highland terrain. Lunar Prospector gamma-ray and neutron spectrometer measurements showed that FeO abundances are highly elevated in the South Pole–Aitken basin and almost reach levels measured in the nearside maria (Lawrence et al., 2002). Other examples for compositional differences apply to thorium, potassium, titanium, magnesium, uranium, and samarium, the

abundances of which are low compared to the abundances found in the nearside maria, but which are distinctly elevated in the South Pole–Aitken basin compared to the surrounding highland terrain (Lawrence et al., 1998; Zhang and Bowles, 2013, and available Lunar Prospector Spectrometer data).

Garrick-Bethell and Zuber (2009) analyzed the structure of the South Pole–Aitken basin based on topography, iron, thorium, albedo and spectral band ratio maps. They showed that the shapes of the boundaries of the low topography and elevated iron and thorium content regions are well described by elliptical shapes that are oriented along the same azimuth, have nearby centers, similar eccentricities, and centers that lie along their common azimuth. In addition, they showed that the albedo and spectral band ratio structures fit well within the topography elliptical shape. Fig. 2 displays four of the five maps used in the analysis by Garrick-Bethell and Zuber (2009). Panel a displays Clementine laser altimeter data, mapped at 0.25 pixel per degree resolution. The Clementine laser altimeter data was acquired from http://pds-geosciences.wustl.edu/missions/clementine/gravtopo.html. Panels b and c display Lunar Prospector gamma-ray spectrometer iron and thorium data, mapped at 0.5 pixel per degree resolution. The Lunar Prospector gamma-ray spectrometer data were obtained from http://pdsgeosciences.wustl.edu/missions/lunarp/reduced_special.html. Panel d displays a global Clementine 750 nm spectral reflectance mosaic which was downloaded from http://astrogeology.usgs.gov.

The South Pole–Aitken basin can, in addition, be easily identified in magnetic field maps, where large clusters of magnetic fields coincide with the northern rim of the basin (e.g. Purucker et al., 2006; Richmond and Hood, 2008; Mitchell et al., 2008; Hood et al., 2013). The origin of these magnetic fields is still under debate. Two currently dominating hypotheses propose quite the opposite: while one proposes that an impact antipodal of the South Pole–Aitken basin is responsible for the magnetic anomalies related to the South Pole–Aitken basin (e.g. Hood et al., 2013), the other proposes that the impact creating the South Pole–Aitken basin itself is associated with the observed magnetic anomalies (e.g. Wieczorek et al., 2012). We show the magnetic field magnitude at 30 km altitude as measured by Lunar Prospector in Fig. 2 panel e. The Lunar Prospector data were obtained from http://pds-geosciences.wustl.edu/missions/lunarp/mager.html.

For comparison, we over-plotted in panels a–e the ellipse fitting the topography data best in white, the respective ellipses fitting the iron and thorium data best in yellow, and the polygon denoting the approximate extension of the ENA feature in red.

4. Discussion

We compare our ENA maps to the individual maps shown in Fig. 2 for the South Pole Aitken basin area. The topography structure of the South Pole–Aitken basin seems well constrained by the ellipse depicted in Fig. 2 panel a. The elevation within this ellipse appears roughly constant, with slightly lower altitudes in the south-eastern part of the South Pole–Aitken basin. The low- and the high-energy ENA maps show reflection ratio reductions that are mostly confined to the north-western and central parts of the ellipse (areas 2 and 5, Fig. 2 panel f), and extend beyond the basin (i.e., the ellipse) northwards to a large part (area 1). Furthermore, while the eastern part of the reduced ENA reflection ratio region is confined to longitudes smaller than −150°, the ellipse reaches −120° in longitude. In addition, north-east of the South Pole–Aitken basin, the elevation map exhibits high

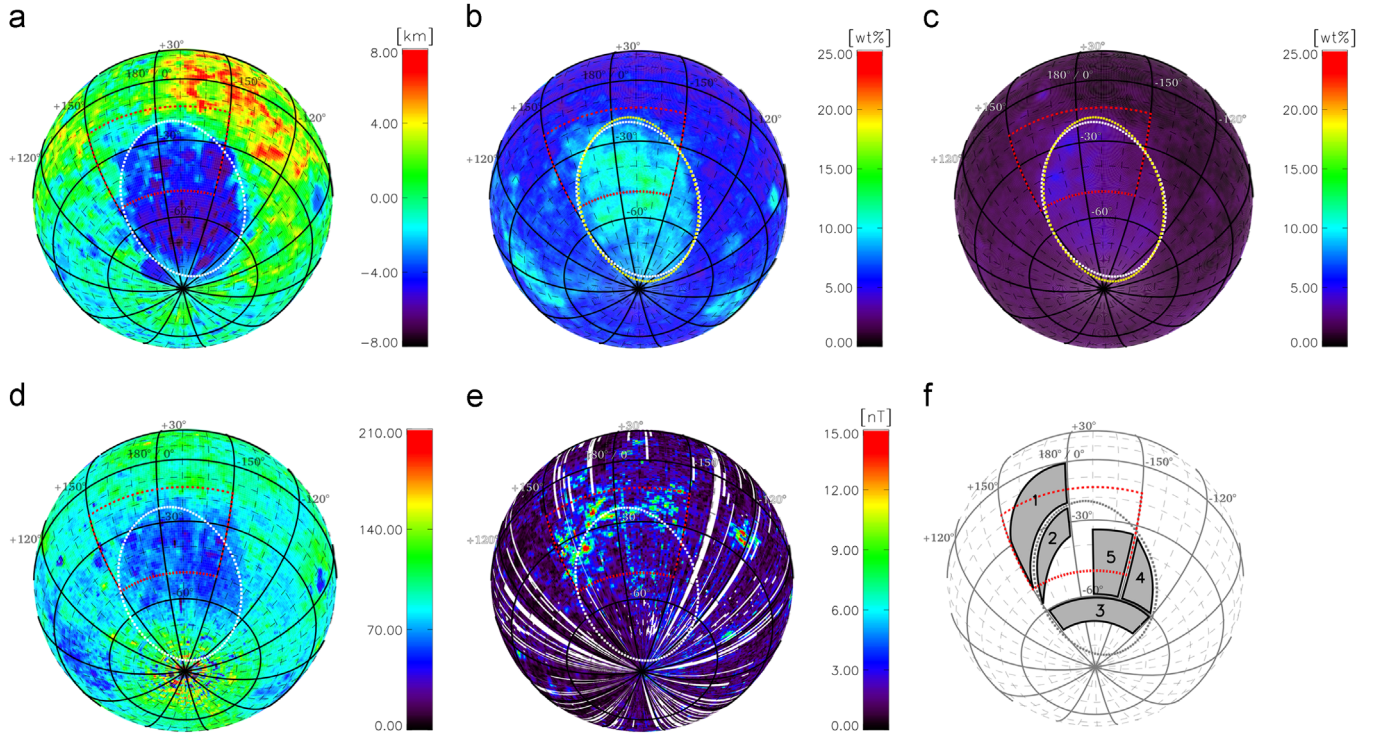

Fig. 2. Maps of the five major features in the South Pole Aitken basin area. Panel a depicts Clementine laser altimeter data, panels b and c display Lunar Prospector gamma-ray spectrometer iron and thorium data, panel d depicts a global Clementine 750 nm spectral reflectance mosaic, and panel e shows the magnetic field at 30 km altitude as measured by Lunar Prospector. In addition, panel f shows five regions of interest: region 1 depicts the area where the ENA feature and the magnetic feature extend beyond the topography feature, regions 2 and 5 depict the areas where the ENA feature and the magnetic field feature coincide with the topography feature, region 3 depicts the area where the topography feature is strong, but not the iron, thorium or albedo feature, and region 4 depicts the area where the topography and the albedo feature are strong, but not the iron or the thorium feature. In all panels, the white (gray) ellipse shows the best fit to the topography data, the red polygon describes the approximate extension of the ENA feature, and in panels b and c the yellow ellipses show the best fits to the respective chemical data.

mountain ranges. The ENA maps show no variation whatsoever in this area.

The areas of iron and thorium abundance enrichments share many characteristics in their selenographic distribution. The centers for the ellipses are almost on top of each other, they differ only by 4.2° in longitude and 2.8° in latitude and the difference in tilt angle is 2.9°. Fig. 2 shows these fits together with the ellipse from topography. The most striking difference between the iron and thorium map is that the iron enrichment with respect to the surrounding terrain is much more distinct: it is in fact more than twice as intense as the thorium enrichment. Both iron and thorium exhibit high abundances confined to the northern halves of the basin (see elemental abundance ellipses in Fig. 2). Their eastern confinement seems to agree better with the ENA feature than the eastern confinement of the topography feature. Again, though, the low-ENA region extends far beyond the elemental abundance regions towards the North.

The visible albedo map exhibits a high correlation with the topography map, but it is not as well defined by the best fit topography ellipse (see Fig. 2 panel d). Especially towards the southern pole, well within the ellipse, the visible albedo increases rather abruptly. This north–south contrast is the only agreement between the visible albedo and the ENA maps, though. Similar to the topography structure, the low-albedo region is very pronounced in the eastern region of the ellipse, where no corresponding ENA feature can be discerned.

The magnetic field measurements in general correlate much better with the two ENA maps than the other previously discussed features. Both the high magnetic field region and the low ENA region cluster around the northern rim of the basin (areas 1 and 2) and are limited to smaller longitudes. In addition, similar to the ENA feature, the magnetic field feature cannot be fitted as well with an ellipse as the other features, but exhibits a more frayed structure. Two regions where the ENA maps and the magnetic field map do not quite agree are the two magnetic anomalies just north of the equator. These two anomalies are very small in extent, though, which could either mean that they are to small to pose an obstacle to the impinging solar wind ions, or that they cannot be resolved with CENA's angular resolution. In addition, they were never directly in CENA's bore-sight, i.e., the counts in these regions are always part of the Gaussian tail distribution over the instrument's field of view (compare Fig. 1 panel c). This could lead to the anomalies being 'washed out' during the mapping process. Overall, the ENA features in either energy range follow quite well variations in the magnetic field strength at 30 km altitude.

In contrast to the Gerasimovich magnetic anomaly (located around −122° longitude/−22° latitude, having a diameter of about 26 km), where the magnetic anomaly is well pronounced in the high energy map but is not visible in the low energy map (Wieser et al., 2009), we see that the South Pole–Aitken basin is well pronounced in both energy ranges (Fig. 1 panels a and b). The cause for the energy dependence at the Gerasimovich anomaly lies in the dependence of the backscattered ENA spectrum on the impinging particle velocity. Futaana et al. (2013) showed that the backscattered ENAs exhibit a Maxwellian energy spectrum with the characteristic energy of $k_BT = 60–160$ eV, which is linearly proportional to the impinging particle velocity. When the solar wind plasma interacts with a weak magnetic field of an anomaly, the protons are decelerated by ambipolar electric field resulting from charge separation of magnetized electrons and non-magnetized ions. The protons reach the surface with lower velocities and result in a spectrum of backscattered ENAs with a lower temperature. The high energy range thus becomes less populated and the respective reflection rate is lower. The magnetic anomaly located at the South Pole–Aitken basin is much larger than the Gerasimovich anomaly (and in fact all other anomalies found on the lunar surface), though: the size of most magnetic anomalies is comparable to the proton gyro radius (Vorburger et al., 2012), whereas the South Pole–Aitken basin spans over an area of about 10 proton gyro radii. The large size could be the reason for the similarity of the low and the high energy ENA maps at the South Pole–Aitken basin, because it allows for magnetic deflection also of decelerated ions at low energy. In addition, the highest fluxes of reflected solar wind ions were observed also in this area (Lue et al., 2011).

A summary of the different surface features for the five different regions depicted in Fig. 2 panel f is given in Table 2, where the numbers correspond to the averages of the respective features within each region. This table shows that the elevation and the visible albedo as well as the iron and the thorium map strongly agree, whereas the magnetic field map and the ENA maps strongly disagree in the analyzed five regions. We also computed the linear Pearson correlation coefficient between the two ENA maps and the other maps based on the values presented in Table 2. The coefficients are presented in Table 3. As one can see, the ENA maps strongly anti-correlate with the magnetic field maps. The only pair with a significant correlation (p-value < 0.05) is the high energy ENA map and the magnetic field map. The low energy ENA map shows a p-value slightly above the significance threshold (p-value$=0.07$). This is in good agreement with the energy dependence of the shielding of magnetic anomalies that was discussed before (Wieser et al., 2009; Vorburger et al., 2012; Kallio et al., 2012).

The considerations above indicate that whereas ENA fluxes are clearly sensitive to magnetic fields located on the lunar surface, they are far less if not non-sensitive to changes in elevation, chemical composition, and visible albedo. Since the ENAs are born from a reflection of a proton on the very surface, i.e., by proton scattering from the atoms on the surface of regolith grains, one would expect that changing the chemical composition of the surface (c.f. iron and thorium maps) should alter the scattering processes. Similarly, the visible albedo is a result of properties of the very surface, e.g. the porosity, surface roughness, chemical composition and others, thus it could have a correlation with the ENA fluxes. The deep basin (elevation map) is the result of a major impact and thus younger than the surrounding lunar high land terrain, less cratered also at very small scales, and the regolith possibly less processed, which could affect the scattering properties of solar wind ions. In all these cases, but the magnetic field, we did not observe a clear correlation, though.

Table 2
Averages of the major features for the five different regions depicted in Fig. 2 panel f. The values are denoted with low, medium, and high according to the following ranges. Elevation: [−8…−2.5, −2.5…2.5, 2.5…8], visible albedo: [< 70, 70…140, > 140], magnetic field: [< 1.5, 1.5…3, > 3], iron: [< 7, 7…9, > 9], thorium: [< 2, 2…3, > 3], ENAs: [< 15, 15…17, > 17].

Region	Elevation (km)	Visible albedo (−)	Magnetic field (nT)	FeO conc. (wt%)	Th conc. (wt%)	ENA low E (−)	ENA high E (−)
(1) North, outside basin	Med (−0.26)	Med (86.45)	High (3.91)	Low (6.60)	Low (1.88)	Low (0.14)	Low (0.13)
(2) North, inside basin	Low (−3.33)	Low (67.44)	High (3.61)	High (9.08)	High (3.53)	Low (0.13)	Low (0.12)
(3) South, inside basin	Low (−5.06)	Med (79.37)	Med (1.87)	Med (8.75)	Med (2.92)	Med (0.16)	Med (0.16)
(4) East, inside basin	Low (−4.72)	Low (63.31)	Med (2.00)	Med (8.64)	Med (2.43)	Med (0.16)	Med (0.16)
(5) Center of basin	Low (−4.80)	Low (56.59)	Med (2.28)	High (10.50)	Med(2.43)	Low (0.14)	Low (0.14)

Table 3
Linear Pearson correlation coefficients computed from the mean values presented in Table 2 for the ENA maps and the other features.

Region	Elevation (km)	Visible albedo (−)	Magnetic field (nT)	FeO conc. (wt%)	Th conc. (wt%)
ENA low E	−0.55	0.02	−0.84	0.01	−0.21
ENA high E	−0.67	−0.14	−0.93	0.20	−0.18

5. Conclusion

We compared our ENA measurements of the South Pole–Aitken basin to topography, albedo, elemental composition and magnetic field measurements of the basin. The comparison shows that whereas the ENAs are sensitive to crustal magnetic fields, they are by far not as sensitive to elevation, visible albedo, and the iron and thorium content. This suggests that the solar wind–lunar surface interaction as observed via ENAs is the same everywhere on the lunar surface irrespective of visible albedo, composition, elevation and that the variation in ENA fluxes is a result of the magnetic fields present on the surface. The flux of backscattered hydrogen ENAs is determined mainly by the impinging plasma flux and ENA imaging of backscattered hydrogen captures the electrodynamics of the plasma at the surface.

The analysis presented in this paper concerns only the total ENA flux. Therefore, we cannot rule out weak dependences of the shape of backscattered ENA spectra and/or scattering function on the surface properties. Studies of such dependences would require ENA instruments with higher energy and angular resolutions than CENA and different observation geometries from the ones provided.

Detailed ENA measurements to study the interaction of solar wind plasma and Mercury's surface are planed within the BepiColombo mission (Benkhoff et al., 2010). An almost identical instrument to CENA (Saito et al., 2010) and another ENA imager at high angular resolution, ELENA (Orsini et al., 2010), will be used for recording the ENA images. Unlike the Moon, Mercury has a dipole magnetic field, which, under nominal conditions, shields a large fraction of the Hermean surface from the solar wind (Kallio and Janhunen, 2003). The open field line in the cusp region, though, allows solar wind protons to precipitate onto the surface (e.g. Kallio and Janhunen, 2003). Imaging of these regions in backscattered hydrogen would reveal the open/closed field line boundary, the plasma precipitation pattern, and magnetospheric dynamics.

Acknowledgments

P. Wurz gratefully acknowledges financial support by the Swiss National Science Foundation.

References

Barabash, S., Bhardwaj, A., Wieser, M., Sridharan, R., Kurian, T., Varier, S., Vijayakumar, E., Abhirami, V., Raghavendra, K.V., Mohankumar, S.V., Dhanya, M.B., Thampi, S., Kazushi, A., Andersson, H., Yoshifumi, F., Holmström, M., Lundin, R., Svensson, J., Karlsson, S., Piazza, D., Wurz, P., 2009. Investigation of the solar wind–Moon interaction onboard Chandrayaan-1 mission with the SARA experiment. Curr. Sci. 96, 526–532.

Benkhoff, J., van Casteren, J., Hayakawa, H., Fujimoto, M., Laakso, H., Novara, M., Ferri, P., Middleton, H.R., Ziethe, R., 2010. BepiColombo—comprehensive exploration of Mercury: mission overview and science goals. Planet. Space Sci. 58, 2–20.

Bhardwaj, A., Barabash, S., Futaana, Y., Kazama, Y., Asamura, K., Sridharan, R., Holmström, M., Wurz, P., Lundin, R., 2005. Low energy neutral atom imaging on the Moon with the SARA instrument aboard Chandrayaan-1 mission. J. Earth Syst. Sci. 114, 749–760.

Crider, D., Vondrak, R., 2002. Hydrogen migration to the lunar poles by solar wind bombardment of the Moon. Adv. Space Res. 30, 1869–1874.

Feldman, W., Lawrence, D., Elphic, R., Barraclough, B., Maurice, S., Genetay, I., Binder, A., 2000. Polar hydrogen deposits on the Moon. J. Geophys. Res. 105, 4175–4176.

Futaana, Y., Barabash, S., Wieser, M., Lue, C., Wurz, P., Vorburger, A., Bhardwaj, A., Asamura, K., 2013. Remote energetic neutral atom imaging of electric potential over a lunar magnetic anomaly. Geophys. Res. Lett. 40, 262–266.

Futaana, Y., Machida, S., Saito, Y., Matsuoka, A., Hayakawa, H., 2003. Moon-related nonthermal ions observed by Nozomi: species, sources and generation mechanism. J. Geophys. Res. 108, 1025.

Garrick-Bethell, I., Zuber, M.T., 2009. Elliptical structure of the lunar South Pole–Aitken basin. Icarus 204, 399–408.

Goswami, J., Annadurai, M., 2009. Chandrayaan-1: India's first planetary science mission to the Moon. Curr. Sci. 96, 486–491.

Halekas, J.S., Poppe, A.R., McFadden, J.P., Glassmeier, K.H., 2013. The effects of reflected protons on the plasma environment of the moon for parallel interplanetary magnetic fields. Geophys. Res. Lett. 40, 4544–4548.

Hood, L.L., Richmond, N.C., Spudis, P.D., 2013. Origin of strong lunar magnetic anomalies: further mapping and examinations of LROC imagery in regions antipodal to young large impact basins. J. Geophys. Res. 118, 1265–1284.

Kallio, E., Janhunen, P., 2003. Solar wind and magnetospheric ion impact on Mercury's surface. Geophys. Res. Lett. 30, 1877.

Kallio, E., Jarvinen, R., Dyadechkin, S., Wurz, P., Barabash, S., Alvarez, F., Fernandes, V.A., Futaana, Y., Harri, A.M., Heilimo, J., Lue, C., Mäkelä, J., Porjo, N., Schmidt, W., Siili, T., 2012. Kinetic simulations of finite gyroradius effects in the lunar plasma environment on global, meso, and microscales. Planet. Space Sci. 74, 146–155.

Kazama, Y., Barabash, S., Wieser, M., Asamura, K., Wurz, P., 2007. Development of an LENA instrument for planetary missions by numerical simulations. Planet. Space Sci. 55, 1518–1529.

Lawrence, D.J., Feldman, W.C., Barraclough, B.L., Binder, A.B., Elphic, R.C., Maurice, S., Thomsen, D.R., 1998. Global elemental maps of the Moon: the Lunar Prospector Gamma-ray Spectrometer. Science 281, 1484.

Lawrence, D.J., Feldman, W.C., Elphic, R.C., Little, R.C., Prettyman, T.H., Maurice, S., Lucey, P.G., Binder, A.B., 2002. Iron abundances on the lunar surface as measured by the Lunar Prospector gamma-ray and neutron spectrometers. J. Geophys. Res. 107, 5130.

Lee, E.M., Gaddis, L.R., Weller, L., Richie, J.O., Becker, T., Shinaman, J., Rosiek, M.R., Archinal, B.A., 2009. A new clementine basemap of the Moon. In: Lunar and Planetary Science Conference, p. 2445.

Lin, R., Mitchell, D., Curtis, D., Anderson, K., Carlson, C., McFadden, J., Acuña, M., Hood, L., Binder, A., 1998. Lunar surface magnetic fields and their interaction with the solar wind: results from Lunar Prospector. Planet. Space Sci. 281, 1480–1484.

Lue, C., Futaana, Y., Barabash, S., Wieser, M., Holmström, M., Bhardwaj, A., Dhanya, M.B., Wurz, P., 2011. Strong influence of lunar crustal fields on the solar wind flow. Geophys. Res. Lett. 38, 3202.

McComas, D., Allegrini, F., Bochsler, P., Frisch, P., Funsten, H., Gruntman, M., Janzen, P., Kucharek, H., Möbius, E., Reisenfeld, D., Schwadron, N., 2009. Lunar backscatter and neutralization of the solar wind: first observations of neutral atoms from the Moon. Geophys. Res. Lett. 36, 12104.

McFadden, L.A.A., Weissman, P.R., Johnson, T.V., 2007. Encyclopedia of the Solar System. Academic Press, San Diego, CA, USA.

Mitchell, D., Halekas, J., Lina, R., Freya, S., Hood, L., Acuña, M., Binder, A., 2008. Global mapping of lunar crustal magnetic fields by lunar prospector. Icarus 194, 401–409.

Niehus, H., Heiland, W., Taglauer, E., 1993. Low-energy ion scattering at surfaces. Surf. Sci. Rep. 17, 213–303.

Orsini, S., Livi, S., Torkar, K., Barabash, S., Milillo, A., Wurz, P., di Lellis, A.M., Kallio, E., The Serena Team, 2010. SERENA: a suite of four instruments (ELENA, STROFIO, PICAM and MIPA) on board BepiColombo-MPO for particle detection in the Hermean environment. Planet. Space Sci. 58, 166–181.

Purucker, M.E., Sabaka, T.J., Halekas, J., Olsen, N., Tsyganenko, N., Hood, L.L., 2006. The lunar magnetic field environment: interpretation of new maps of the internal and external fields. In: Mackwell, S., Stansbery, E. (Eds.), 37th Annual Lunar and Planetary Science Conference, p. 1933.

Richmond, N., Hood, L., 2008. A preliminary global map of the vector lunar crustal magnetic field based on Lunar Prospector magnetometer data. J. Geophys. Res. 113, 2010.

Saito, Y., Sauvaud, J.A., Hirahara, M., Barabash, S., Delcourt, D., Takashima, T., Asamura, K., BepiColombo MMO/MPPE Team, 2010. Scientific objectives and instrumentation of Mercury Plasma Particle Experiment (MPPE) onboard MMO. Planet. Space Sci. 58, 182–200.

Saito, Y., Yokota, S., Tanaka, T., Asamura, K., Nishino, M.N., Fujimoto, M., Tsunakawa, H., Shibuya, H., Matsushima, M., Shimizu, H., Takahashi, F., Mukai, T., Terasawa, T., 2008. Solar wind proton reflection at the lunar surface: low energy ion measurement by MAP-PACE onboard SELENE (KAGUYA). Geophys. Res. Lett. 35, 24205.

Vorburger, A., Wurz, P., Barabash, S., Wieser, M., Futaana, Y., Holmström, M., Bhardwaj, M., Asamura, K., 2012. Energetic neutral atom observations of magnetic anomalies on the lunar surface. J. Geophys. Res. 117, 7208.

Vorburger, A., Wurz, P., Barabash, S., Wieser, M., Futaana, Y., Holmström, M., Bhardwaj, A., Asamura, K., 2014. First direct observation of sputtered lunar oxygen. J. Geophys. Res. (Space Phys.) 119, 709–722.

Vorburger, A., Wurz, P., Barabash, S., Wieser, M., Futaana, Y., Lue, C., Holmström, M., Bhardwaj, A., Dhanya, M.B., Asamura, K., 2013. Energetic neutral atom imaging of the lunar surface. J. Geophys. Res. 118, 3937–3945.

Wang, X.D., Bian, W., Wang, J.S., Liu, J.J., Zou, Y.L., Zhang, H.B., Lü, C., Liu, J.Z., Zuo, W., Su, Y., Wen, W.B., Wang, M., Ouyang, Z.Y., Li, C.L., 2010. Acceleration of scattered solar wind protons at the polar terminator of the Moon: results from Chang'E-1/SWIDs. Geophys. Res. Lett. 37, 7203.

Wieczorek, M.A., Weiss, B.P., Stewart, S.T., 2012. An impactor origin for lunar magnetic anomalies. Science 335, 1212–1215.

Wieser, M., Barabash, S., Futaana, Y., Holmström, M., Bhardwaj, A., Sridharan, R., Dhanya, M., Schaufelberger, A., Wurz, P., Asamura, K., 2010. First observation of a mini-magnetosphere above a lunar magnetic anomaly using energetic neutral atoms. Geophys. Res. Lett. 37, 5103.

Wieser, M., Barabash, S., Futaana, Y., Holmström, M., Bhardwaj, A., Sridharan, R., Dhanya, M., Wurz, P., Schaufelberger, A., Asamura, K., 2009. Extremely high reflection of solar wind protons as neutral hydrogen atoms from regolith in space. Planet. Space Sci. 57, 2132–2134.

Zhang, W., Bowles, N.E., 2013. Mapping lunar TiO_2 and FeO with M3 data. In: European Planetary Science Congress 2013, vol. 8, p. 374.